



Structure and conductivity in iron-doped $\text{Bi}_{26}\text{Mo}_{10}\text{O}_{69-\delta}$

Z. A. Mikhaylovskaya¹ · S. A. Petrova² · I. Abrahams³ · E. S. Buyanova¹ · M. V. Morozova¹ · D. G. Kellerman^{1,4}

Received: 27 December 2017 / Revised: 19 March 2018 / Accepted: 25 March 2018 / Published online: 4 May 2018

© Springer-Verlag GmbH Germany, part of Springer Nature 2018

Abstract

A series of complex oxides of general formula $\text{Bi}_{26}\text{Mo}_{10-2x}\text{Fe}_{2x}\text{O}_{69-3x}$ was synthesized and studied. The solid solution formation ranges and polymorphic modification limits were determined. SEM investigations and chemical analysis showed homogenous samples and confirmed the theoretical concentrations of the dopant. High-resolution neutron and X-ray diffraction were used to describe the structural features of the solid solution at ambient and high temperatures (30–800 °C). Structure refinement was carried out by Rietveld analysis using a combination of X-ray and backscattered neutron data. Close inspection of the fit at room temperature revealed a non-centrosymmetric $P1$ space group and additional peaks associated with oxygen and/or magnetic ordering. Magnetic measurements showed the samples had low magnetic susceptibility and a magnetic transition at ~ -20 °C. A.C. impedance spectroscopy was used to determine the electroconductive properties of $\text{Bi}_{26}\text{Mo}_{10-2x}\text{Fe}_{2x}\text{O}_{69-3x}$. Two basic types of impedance curves were detected at low and high temperatures, correlated with a change from triclinic to monoclinic symmetry. Details of both the monoclinic and triclinic structures are discussed, with the variation of electroconductive properties explained by structural changes.

Keywords Bismuth molybdate · Oxide ion conductor · Neutron diffraction · A.C. impedance spectroscopy

Introduction

Fast oxide ion-conducting solid electrolytes based on bismuth oxide are being studied as potential materials for use in a variety of electrochemical devices such as solid oxide fuel cells [1] and gas separation membranes [2]. They also have important catalytic properties [3–5]. As ionic conductors,

these materials can be classified according to their dimensionality, as one dimensional, e.g., $\text{Bi}_{26}\text{Mo}_{10}\text{O}_{69-\delta}$ [6]; two dimensional, e.g., the BIMEVOXes [7]; and three dimensional, e.g., $\delta\text{-Bi}_2\text{O}_3$ [8].

The one-dimensional conductor, $\text{Bi}_{26}\text{Mo}_{10}\text{O}_{69-\delta}$, was first described by Vannier et al. [6] and later by Buttery et al. [9] as part of a solid solution with Bi:Mo ratios ranging from 2.6 to 2.8 (i.e., 56.5 to 58.3% Bi_2O_3). Later studies by Galy et al. [10] extended this range from 2.534 to 3.4 (i.e., 55.9 to 63.6% Bi_2O_3). However, a more recent work has shown a number of room temperature stable phases in the Bi:Mo range 2.67 to 3.4 (i.e., 57.1 to 63.6% Bi_2O_3), which transform to the columnar structure at temperatures above ca. 650 °C [11].

The structure of $\text{Bi}_{26}\text{Mo}_{10}\text{O}_{69-\delta}$ was first determined in the monoclinic space group $P2_1/c$ by Buttery et al. [9], who noted a small triclinic distortion. A later work by Vannier et al. confirmed the basic structure, which consists of columns of $[\text{Bi}_{12}\text{O}_{14}]_n^{8n+}$, separated by an apparently isolated Bi^{3+} cation and five $[\text{MoO}_4]^{2-}$ tetrahedra [6]. This accounts for 68 of the 69 oxygen atoms per cell and there has been some debate as to the location of the 69th oxygen required to maintain electroneutrality, if the cations are assumed to be in their nominal oxidation states of +3 and +6 for bismuth and molybdenum, respectively. More recently, the triclinic structure of $\text{Bi}_{26}\text{Mo}_{10}\text{O}_{69-\delta}$

Electronic supplementary material The online version of this article (<https://doi.org/10.1007/s11581-018-2543-1>) contains supplementary material, which is available to authorized users.

✉ Z. A. Mikhaylovskaya
zoya.mihaylovskaya@urfu.ru

¹ Ural Federal University, Lenin Ave. 51, 620000 Ekaterinburg, Russia

² Institute for Metallurgy, Ural Branch of the Russian Academy of Sciences, 101 Amundsen Str, 620016 Ekaterinburg, Russia

³ Materials Research Institute, School of Biological and Chemical Sciences, Queen Mary University of London, Mile End Road, London E1 4NS, UK

⁴ Institute of Solid State Chemistry, Ural Branch of the Russian Academy of Sciences, 91, Pervomayskaya St, 620990 Ekaterinburg, Russia

has been elucidated by Ling et al. [12] using a combination of X-ray and neutron scattering methods, as well as molecular dynamics calculations. They found the coexistence of both 4- and 5-coordinate molybdate polyhedra, with rotational disorder of these above 310 °C, consistent with a conduction mechanism involving diffusive jumps between the bismuthate columns via the molybdate polyhedra [13].

Since the discovery of fast ion conduction in these materials, there have been a number of studies on substitution of both molybdenum and bismuth by a variety of cations such as Ca^{2+} , Sr^{2+} , Ba^{2+} , Pb^{2+} , Mn^{2+} , Al^{3+} , Ge^{4+} , P^{5+} , V^{5+} , W^{6+} , Cr^{6+} , and Y^{3+} and various lanthanides [14–17]. Changes in electrical conductivity, both increases and decreases, result from these substitutions. In the present work, we examine low levels of iron substitution in $\text{Bi}_{26}\text{Mo}_{10}\text{O}_{69-3x}$, including detailed structural characterization of both the monoclinic and triclinic phases using high-resolution neutron diffraction. The phase behavior as a function of composition and temperature is examined with respect to changes in magnetic and electrical properties.

Experimental

Sample preparation

Samples of composition $\text{Bi}_{26}\text{Mo}_{10-2x}\text{Fe}_{2x}\text{O}_{69-3x}$ ($0.0 \leq x \leq 0.4$) were synthesized by conventional solid state methods from the precursor oxides. Stoichiometric amounts of dried powders of Bi_2O_3 (99.9%), MoO_3 (99.5%), and Fe_2O_3 (96%) were weighed and mixed in an agate mortar as a dispersion in ethanol. The dried mixture was pelletized at 20 bar using a uniaxial press to yield pellets of 20 mm diameter. The pellets were placed on an alumina plate in a bed of precursor powder and heated at 550 °C for 48 h, then quenched in water to room temperature. The samples were then reground in ethanol, dried, pelletized once more, and reheated to 850 °C for 24 h, before slow cooling in air to room temperature over a period of approximately 12 h.

For impedance measurements, the synthesized samples were pelletized at 20 bar to yield pellets of 10 mm diameter and ca. 2.5 mm thickness. The pressed pellets were then heated to 850 °C for 24 h, before slow cooling in air to room temperature. Pt electrodes were applied by decomposition of a dispersion of $\text{NH}_4(\text{PtCl}_6)$ at ca. 400 °C.

Morphology and composition measurements

The morphology of the obtained powders was studied using scanning electron microscopy (SEM) with a JEOL JSM 6390LA and chemical composition analyzed with a JED 2300 EDX-analyzer. Dopant concentration in $\text{Bi}_{26}\text{Mo}_{10-2x}\text{Fe}_{2x}\text{O}_{69-3x}$ was monitored by chemical analysis of the

samples. Powder samples of $\text{Bi}_{26}\text{Mo}_{10-2x}\text{Fe}_{2x}\text{O}_{69-3x}$ were weighed, dissolved in a mixture of concentrated hydrochloric and nitric acids, and made up to 100 ml volume with distilled water. Iron concentrations in the obtained solutions were determined by atomic absorption spectral analysis using a Solaar M6 spectrometer (Thermo Scientific) by the standard addition method.

Impedance measurements

Impedance spectra were measured on an Elins Z-3000 impedance spectrometer, over the frequency ranges 1 MHz to 0.1 Hz and 3 MHz to 10 Hz, at stabilized temperatures from ca. 225 °C to ca. 850 °C. Two cycles of heating and cooling were performed. Data presented correspond to the second cooling run. Data were modeled using equivalent electrical circuits with the Zview software (Version 2.6b, Scribner Associates, Inc.).

Magnetic measurements

The magnetization curves of $\text{Bi}_{26}\text{Mo}_{10-2x}\text{Fe}_{2x}\text{O}_{69-3x}$ ($x = 0.1, 0.3$) powders were collected with a VSM-5T (Cryogenic Ltd.) vibrating sample magnetometer in the temperature range 4 to 300 K and in fields up to 5 T. The thermal variation of magnetic susceptibility was modeled with Curie–Weiss law. The effective magnetic moments were calculated from the Curie constant $\mu_{\text{eff}} = \sqrt{8C}$. The oxidation state of iron was calculated from theoretical μ_{eff} values of Fe^{2+} and Fe^{3+} ions:

$$\mu_{\text{eff}}^2 = \mu_{\text{eff}}^{2\text{Fe}^{3+}} \cdot c_{\text{Fe}^{3+}} + \mu_{\text{eff}}^{2\text{Fe}^{2+}} \cdot (1 - c_{\text{Fe}^{3+}}) \quad (1)$$

where $c_{\text{Fe}^{3+}}$ is the molar concentration of Fe^{3+} ions, and $(1 - c_{\text{Fe}^{3+}})$ is the molar concentration of Fe^{2+} ions.

Diffraction

X-ray powder diffraction data were obtained on a PANalytical X'Pert Pro diffractometer fitted with an X'Celerator detector and a Bruker Advance D8 diffractometer with a VANTEC1 detector. In both cases, Ni-filtered $\text{Cu-K}\alpha$ radiation ($\lambda_1 = 1.54056 \text{ \AA}$ and $\lambda_2 = 1.54439 \text{ \AA}$) was used. Data were collected in flat plate θ/θ geometry and calibrated against external LaB_6 and SRM1976 (Al_2O_3) standards for the X'Pert and D8 diffractometers, respectively. Room temperature data suitable for detailed Rietveld refinement were collected in the 2θ range 5° – 120° , in steps of 0.0167° , with an effective scan time of 200 s per step. Elevated temperature measurements on the D8 instrument were carried out using an Anton-Paar XRK-900 or HTK-1200 cameras in steps of 10°C on heating and 50°C on cooling. For Rietveld analysis, elevated temperature measurements were performed on the X'Pert Pro diffractometer using an Anton-Paar HTK15 camera at 50°C intervals from 100 to

800 °C on heating and cooling. Data were collected in the 2θ range 5° – 120° , in steps of 0.033° , with an effective scan time of 50 s per step for all but the data at 800 °C, where the room temperature scan parameters were used.

Neutron powder diffraction data were obtained on the HRPD diffractometer at the ISIS Facility, Rutherford-Appleton Laboratory, for the $x = 0.1$ and $x = 0.3$ compositions. Data were collected on backscattering (ca. 168°), 90° , and low-angle (ca. 30°) detectors. For the $x = 0.1$ composition, measurements were performed with the powdered sample contained directly in a cylindrical vanadium can (11 mm diameter) located in front of the backscattering detectors, inside an evacuated furnace with vanadium windows. For the $x = 0.3$ composition, the sample was first sealed in a 10-mm-diameter silica tube, which was then placed in an 11-mm-diameter vanadium can in the furnace. Data were collected at room temperature and at 50 °C intervals from 300 to 750 °C and 200 to 700 °C for the $x = 0.1$ and $x = 0.3$ samples, respectively. At room temperature and at 650 °C, longer data collections of 200 $\mu\text{A h}$ and 150 $\mu\text{A h}$, respectively, were made, while at other temperatures, shorter collections of between 20 and 30 $\mu\text{A h}$ were performed.

Structure refinement was carried out by Rietveld analysis with the GSAS suite of programs [18], using a combination of equally weighted X-ray and backscattered neutron data sets where available and the X-ray data sets alone for other refinements. Initial starting models were based on the structure of monoclinic $\text{Bi}_{26}\text{Mo}_{10}\text{O}_{69}$ reported by Vannier et al. [6] and the triclinic model of Ling et al. [12]. For the $x = 0.3$ composition, $\text{Bi}_6\text{Mo}_2\text{O}_{15}$ [19] was included as a secondary phase at temperatures from 600 to 750 °C. Independent isotropic displacement parameters were refined for all atoms at room temperature, while those for like atoms were tied in the refinements of the high-temperature models. Fe was initially assumed to be randomly distributed across all Mo sites. However, site occupancy refinement confirmed a preferential distribution and this was fixed in the final refinements. Crystal and refinement parameters for the $x = 0.1$ and 0.3 compositions at room temperature and 650 °C are given in the supplementary information as Tables S1 and S2, respectively, along with the refined structural parameters (Tables S3 to S6) and the corresponding fitted diffraction profiles are given in Figs. S1 and S2.

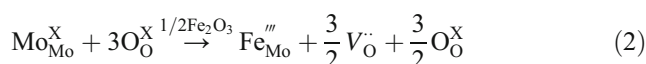
Results and discussion

Solid solution formation

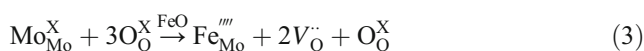
Substitution of molybdenum by iron in the $\text{Bi}_{26}\text{Mo}_{10-2x}\text{Fe}_{2x}\text{O}_{69-3x}$ system yielded samples with X-ray diffraction patterns similar to those of the unsubstituted parent compound, up to $x = 0.30$ (Fig. 1). Above $x = 0.30$, additional peaks corresponding to $\text{Bi}_{38}\text{Mo}_7\text{O}_{78}$ [20] are evident. The data

for all compositions were indexed using the triclinic cell, as previously suggested for the unsubstituted parent compound [9] and recently described in detail by Ling et al. [12].

The variation of unit cell parameters with composition is given in the supplementary information as Table S7. The unit cell volume is seen to decrease with increasing value of x . This decrease in volume is somewhat unexpected, since substitution of the smaller Mo^{6+} ion by the larger Fe^{3+} ion (with ionic radii of 0.41 and 0.49 Å, respectively, for four coordinate geometry [21]) should lead to an increase in cell volume. In order to explain this apparent anomaly, it is helpful to consider the solid solution mechanism in the present system, which may be written as:



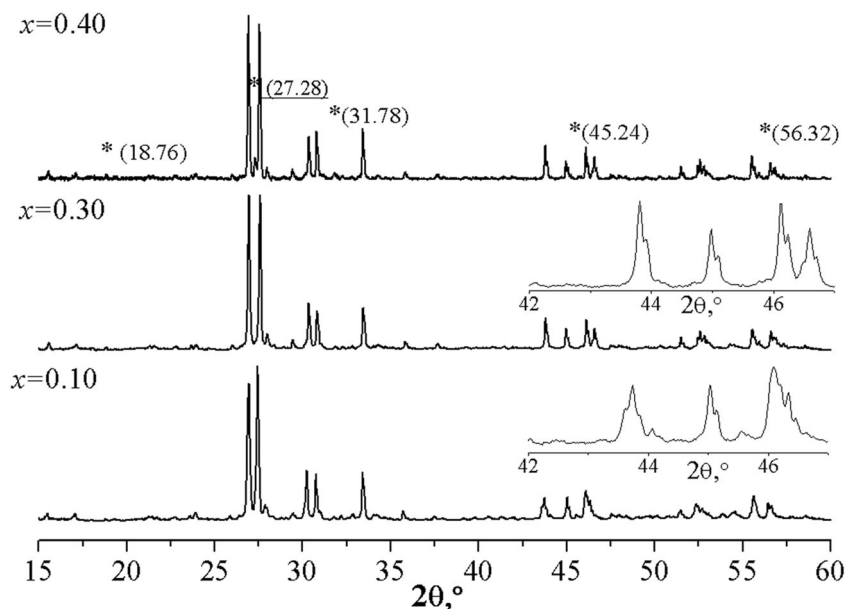
Thus, the substitution of Mo^{6+} by Fe^{3+} is accompanied by creation of oxide ion vacancies, which would be expected to result in a decrease in volume. Often, iron shows a mixed oxidation state, and as a result, Fe^{2+} can also be present in complex oxides. It shows a similar solid solution mechanism and a decrease in volume is also expected:



As is seen in Table S11, the decrease in volume (-0.29% from $x = 0.00$ to $x = 0.30$) is mainly attributed to the decreases in the a -cell parameter (-0.45% from $x = 0.00$ to $x = 0.30$), with that for the c -axis showing an increase with an increasing level of substitution ($+0.27\%$ from $x = 0.00$ to $x = 0.30$). The b -dimension is mainly associated with the axial dimension of the bismuthate columns and changes only slightly, suggesting that the volume change is mostly attributable to any change of the a and c parameters, i.e., in the intercolumnar spacing, consistent with loss of oxide ions from between the columns and intercalation of the larger ion. A similar regularity of the changes of parameters (a decreases, b changes slightly, c increases, V decreases) is observed in [15], where the substitution of isolated Bi^{3+} by bigger ions of Ba^{2+} , Pb^{2+} , and Sr^{2+} is described. This would readily be accomplished by loss of the “69th” oxide ion, identified by Ling et al. [12] as lying between molybdate polyhedra and would lower the coordination number of some of the Mo/Fe atoms from 5 to 4, with a resultant shrinkage of the lattice. If correct, then the solid solution limit could be predicted to occur when all the Mo/Fe atoms were tetrahedral, i.e., when there were no further oxide ions in the 69th position, which is calculated to occur at $x = 0.33$. This is consistent with the present results, which show that the solid solution limit lies between $x = 0.30$ and $x = 0.35$.

The variation in the cell angles α and γ shows that at $x = 0.30$, the cell approaches monoclinic dimensions. However, Rietveld analysis confirms a small triclinic distortion remains.

Fig. 1 Detail of diffraction patterns for compositions of general formula $\text{Bi}_{26}\text{Mo}_{10-2x}\text{Fe}_{2x}\text{O}_{69-3x}$. Peaks associated with $\text{Bi}_{38}\text{Mo}_7\text{O}_{78}$ are indicated with an asterisk



Ambient temperature structures

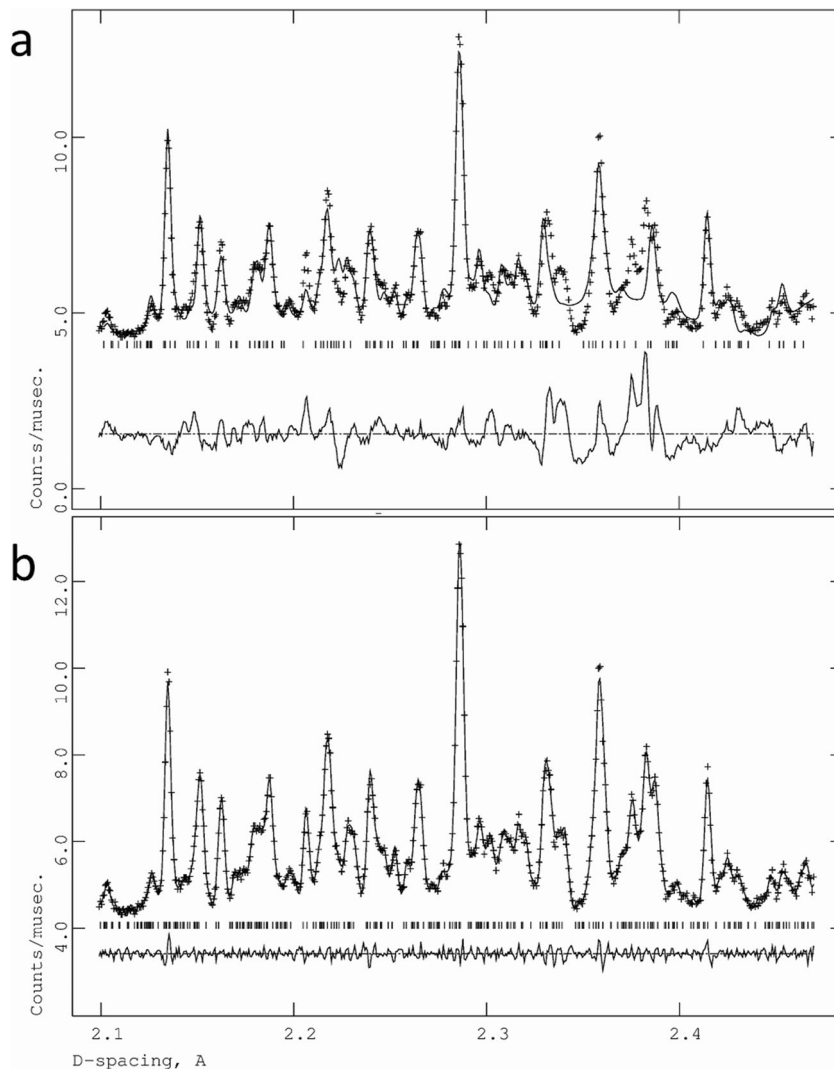
The data for the $x = 0.10$ composition were initially fitted using the triclinic model proposed by Ling et al. [12]. However, despite resulting in a satisfactory fit to the data, it was evident that two of the Bi positions, Bi(13) and Bi(14) in the original model, located on the $1a$ and $1b$ positions, respectively, of the $P-1$ space group, showed unrealistic coordination environments. In addition, the isotropic thermal parameter for oxygen, although within acceptable limits, was significantly larger than those refined for the cations, suggesting some positional disorder in the oxide ion sublattice. Refinement of the Bi(13) and Bi(14) atomic coordinates disordered over general positions resulted in more satisfactory coordination environments for these atoms. The presence of such disorder suggests a breaking of the centrosymmetric condition. In order to establish whether the structure was truly non-centrosymmetric, a model was constructed and refined in space group $P1$. To facilitate refinement of such a large number of variables, the maximum atomic shift between cycles was set to 0.02 \AA , and a large number of refinement cycles was carried out to ensure satisfactory convergence. As for the refinement in space group $P-1$, soft restraints were applied to the Mo-O distances to ensure realistic molybdate coordination polyhedra. Since the non-centrosymmetric analysis involves many more variable parameters, it is necessary to check the statistical significance of any improvement in R -factors. The best fit obtained in space group $P-1$ had 220 variable parameters for 10,799 data points and yielded an overall weighted profile R -factor of 0.0325. The refinement in space group $P1$ utilized 369 parameters and gave an improved overall weighted profile R -factor of 0.0267. Using the method of Hamilton [22] and extrapolation for the dimensions of the current system, the R -factor ratio

of 1.217 is much larger than the extrapolated F value of 1.049 at the 99.5 significance level, indicating that the observed improvement in R -factor is statistically significant.

Close inspection of the fit to the high-resolution neutron data for the $x = 0.10$ composition revealed significant differences in the observed and calculated patterns (Fig. 2a). Additional peaks could not be attributed to likely impurities and were not evident in the patterns at high temperatures. These additional peaks can be indexed through a doubling of the a -axis and a LeBail refinement in the resulting supercell ($a = 23.5936(5) \text{ \AA}$, $b = 5.8058(1) \text{ \AA}$, $c = 24.7649(5) \text{ \AA}$, $\alpha = 89.897(1)^\circ$, $\beta = 102.904(1)^\circ$, and $\gamma = 89.920(1)^\circ$) gave a very good fit (Fig. 2b). The corresponding X-ray data show no additional peaks and suggests that if indeed a superlattice is present, then it is likely associated either with ordering in the oxide ion sublattice or with possible magnetic ordering of Fe atoms (see below). Although the structure can be modeled in the supercell, in the case of ordering in the oxide ion sublattice, the number of variable parameters involved is very large, making a meaningful refinement difficult and therefore only the subcell model is presented here.

Independent refinement of the isotropic displacement parameter for O(69) on the position proposed by Ling et al. [12] at 0.5, 0.0, and 0.5 led to very high values for this parameter. Furthermore, when the occupancy of this site was refined, a negative value was obtained. Attempts to refine oxide ion occupancy on similar sites in the structure yielded significant positive scattering density around 0.5, 0.0, and 0.0, which was then allowed to refine as a general position in the $P1$ space group. In the final refinement, the occupancy on this site was fixed at the stoichiometric value. O(69) was found to be coordinated to Mo(3) at a distance of 2.105 \AA , resulting in a distorted trigonal bipyramidal coordination for Mo(3), and

Fig. 2 Details of the fitted neutron diffraction patterns for the $x = 0.1$ composition showing **a** Rietveld analysis using the cell proposed by Buttery et al. [9] and **b** LeBail fit using a $2a$ supercell model. Observed (plus signs), calculated (line), and difference (lower) profiles are shown, with reflection positions indicated by markers



contacts of 2.540 Å and 2.857 Å to Bi(11) and Mo(8), respectively (Fig. 3a). In this respect, it therefore resembles the model presented by Ling et al. [12], which showed both 4- and 5-coordinate Mo polyhedra. Mixtures of Mo coordination environments can be observed in other oxide ion-conducting systems such as a $\text{La}_2\text{Mo}_2\text{O}_9$ [23]. Iron was found to be preferentially located on the Mo(2) site. In the present work, the molybdate polyhedra show extensive distortion away from tetrahedral geometry Fig. 3b. These distortions can be quantified using a bond-length distortion index (DI). In [24], three types of DI were suggested:

$$DI(TO) = \frac{\sum_{i=1}^{i=n} |TO_i - \langle TO \rangle|}{n^* \langle TO \rangle} \quad (4)$$

where TO_i is the i th M-O bond length in an MO_n polyhedron and $\langle TO \rangle$ is the average M-O bond length in this MO_n polyhedron;

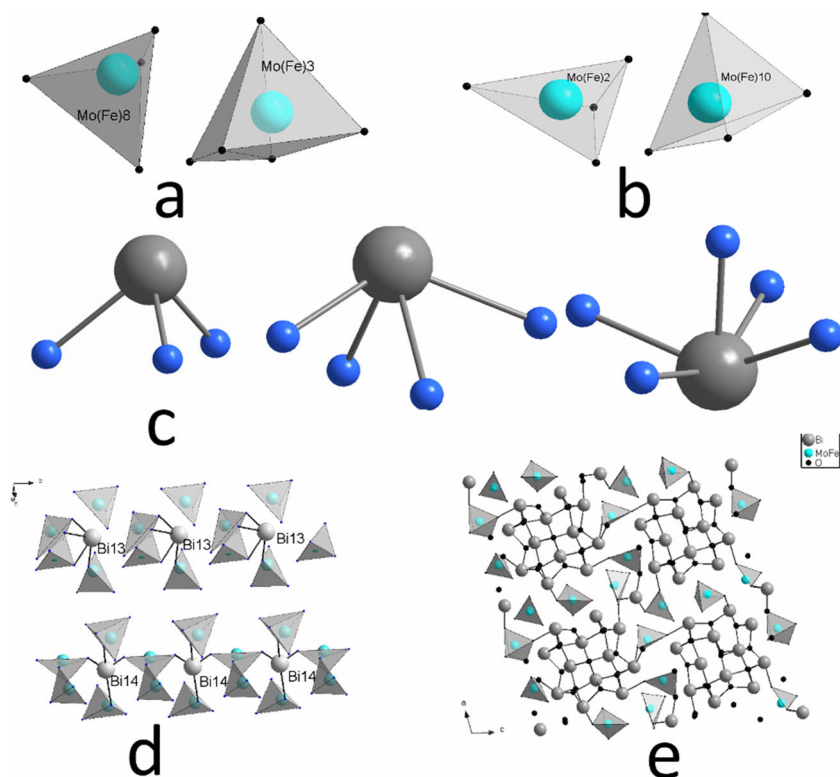
$$DI(OTO) = \frac{\sum_{i=1}^{i=m} |OTO_i - \langle OTO \rangle|}{m^* \langle OTO \rangle} \quad (5)$$

where OTO_i is the i th O-M-O angle in MO_n polyhedron and $\langle OTO \rangle$ is the average O-M-O angle in this MO_n polyhedron containing m O-M-O angles and

$$DI(OO) = \frac{\sum_{i=1}^{i=l} |OO_i - \langle OO \rangle|}{l^* \langle OO \rangle} \quad (6)$$

where OO_i is the i th O-O distance in MoO_n polyhedron and $\langle OO \rangle$ is the average O-O distance in this MO_n polyhedron containing l O-O edges. Values of DI for the studied compositions are given in Table 1. Since the angles are independent, the $DI(TO)$ index is universal for all types of symmetrical polyhedra, and its use for comparison of polyhedral distortion in $\text{Bi}_{26}\text{Mo}_{10-2x}\text{Fe}_{2x}\text{O}_{69-3x}$ is most reasonable. In all cases, the $DI(TO)$ values for the $x = 0.3$ composition were greater than

Fig. 3 **a** Trigonal bipyramidal coordination of Mo(3) and typical tetrahedral coordination of Mo; **b** examples of extensive distortion MoO₄ polyhedra from tetrahedral geometry; **c** trigonal pyramidal, four pyramidal, and truncated octahedral coordination of Bi; **d** coordination of isolated Bi(13) and Bi(14); **e** structure of Bi₂₆Mo_{9.8}Fe_{0.2}O_{68.7} in general



the corresponding values for $x = 0.1$.

Bismuth atoms in Bi₂₆Mo_{9.8}Fe_{0.2}O_{68.7} exhibit distorted coordination environments reflecting the stereochemical activity of the $6s^2$ lone pair of electrons, with three to five shorter bonding interactions and several essentially non-bonding contacts. Three basic coordination environments are observed, trigonal pyramidal, four pyramidal, and truncated octahedral, representative examples of which are shown in Fig. 3c. The two intercolumnar bismuth atoms, Bi(13) and Bi(14), show four pyramidal and trigonal pyramidal coordination geometries, respectively (Fig. 3d) and are located centrally between four [Bi₁₂O₁₄]_n columns (Fig. 3e).

As for the $x = 0.10$ composition, the diffraction data for the $x = 0.30$ composition were modeled using the non-centrosymmetric triclinic model in *P1*. The statistical significance of the fit to the non-centrosymmetric model compared to that in the centrosymmetric space group was confirmed using the method of Hamilton [22] as for the $x = 0.10$ composition. The R-factor ratio was 1.155 and extrapolation for the dimensions of the current system gave an *F* value of 1.049 at the 99.5 significance level indicating that the observed improvement in R-factor is statistically significant. The location of the 69th oxide ion could not be unambiguously determined. If as discussed above, electroneutrality of the system is

Table 1 Values of distortion indices for Bi₂₆Mo_{10-2x}Fe_{2x}O_{69-3x}

Compound	Bi ₂₆ Mo _{9.8} Fe _{0.2} O _{68.7}			Bi ₂₆ Mo _{9.4} Fe _{0.6} O _{68.1}		
	DI (T-O)	DI (O-T-O)	DI (O-O)	DI (T-O)	DI (O-T-O)	DI (O-O)
Mo1(Fe1)O ₄	0.038	0.077	0.062	0.077	0.065	0.061
Mo2(Fe2)O ₄	0.048	0.106	0.088	0.130	0.115	0.099
Mo3(Fe3)O ₅	0.039	0.170	0.127	0.120	0.070	0.040
Mo4(Fe4)O ₄	0.032	0.123	0.097	0.174	0.183	0.212
Mo5(Fe5)O ₄	0.039	0.209	0.148	0.070	0.246	0.161
Mo6(Fe6)O ₄	0.039	0.099	0.075	0.088	0.118	0.056
Mo7(Fe7)O ₄	0.061	0.207	0.121	0.090	0.134	0.073
Mo8(Fe8)O ₄	0.081	0.092	0.051	0.090	0.051	0.056
Mo9(Fe9)O ₄	0.061	0.152	0.109	0.103	0.118	0.087
Mo10(Fe10)O ₄	0.008	0.168	0.121	0.041	0.143	0.107

maintained through loss of the 69th oxide ion, then at the $x = 0.30$ composition, the calculated occupancy for this site is 0.10, which, bearing in mind the low symmetry and complexity of the present structure, is likely beyond the limits of detection with the present data.

All the Mo/Fe atoms show distorted tetrahedral geometry. The values for the tetrahedral distortion parameters indicate that the tetrahedra are more distorted than at the $x = 0.10$ level of substitution. At the $x = 0.30$ composition, the bismuth coordination environments are similar to those found at the $x = 0.10$ composition.

Thermal variation of structure

The thermal variation of unit cell volume for the two studied compositions is shown in Fig. 4. For the $x = 0.10$ composition, there is a step in the thermal expansion of unit cell volume between 300 and 350 °C, associated with a change from triclinic to monoclinic symmetry, as previously described for the unsubstituted parent compound [12]. On cooling, the reverse transition occurs at lower temperature, between 250 and 200 °C. This hysteresis is significantly reduced when measurements are performed using a 10 °C step. Interestingly, the lattice parameters on cooling were found to be slightly lower than those observed on heating, which may be indicative of a change in oxygen stoichiometry, with the sample exhibiting a greater degree of oxidation on cooling. For the $x = 0.30$ composition, volume change is fully reproducible between heating and cooling runs. The triclinic to monoclinic phase transition occurs between 150 and 200 °C. The unit cell parameters α and γ increase gradually from 89.97° and 89.93° (at 150 °C) to 89.98° and 89.99° (at 200 °C) and 89.999° and 89.991° (at 250 °C) and clear change in slope or step is not observed. As a result, the monoclinic structure was used for calculations above 250 °C. However, a change in slope is

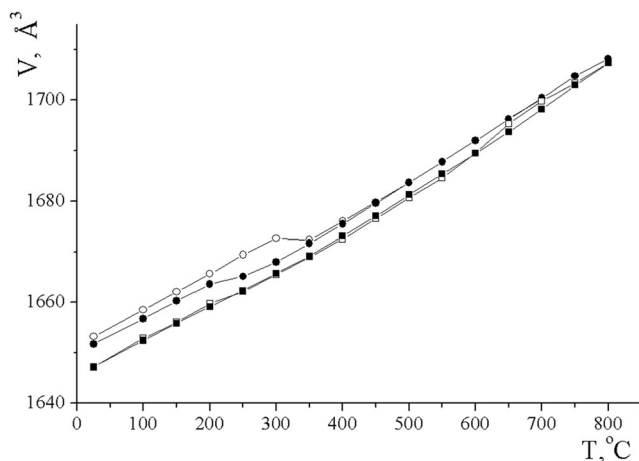


Fig. 4 Thermal variation of unit cell volume in $\text{Bi}_{26}\text{Mo}_{10-2x}\text{Fe}_{2x}\text{O}_{69-3x}$ for $x = 0.1$ (squares) and $x = 0.3$ (triangles) on heating (open symbols) and cooling (filled symbols)

observed above ca. 600 °C and is accompanied by the appearance of additional peaks in the diffraction patterns, attributable to Bi_2MoO_6 [25] and Fe_2O_3 [26] (Fig. 5). These additional phases disappear at around 800 °C and are absent on cooling. Interestingly, in the second and third heating–cooling cycles under identical conditions, phase separation was detected over a narrower temperature range (710–800 °C). Additionally, high-temperature X-ray diffraction data for the $x = 0.20$ composition also showed the appearance of low concentrations of Bi_2MoO_6 and Fe_2O_3 phases. Only a slight deviation of unit cell parameters was observed (Supplementary Information Fig. S3), with a maximum deviation in second and further heating–cooling cycles of 0.05–0.3% for the β parameter. As a result, the plot of volume contraction on cooling for this composition suggests that the phase separation seen on initial heating leaves the overall stoichiometry of the principal phase relatively unaffected.

For the $x = 0.10$ and $x = 0.30$ compositions at 650 °C, the 69th oxide ion (O(19)) is found to be coordinated to Mo(2), yielding a distorted trigonal bipyramidal coordination, analogous to the situation at room temperature (Fig. 6a). The distortion indices for the tetrahedral $\text{Mo(Fe)}\text{O}_n$ polyhedra (Table 2) indicate that they are less distorted than those at room temperature. The high DI for $\text{Mo}_2(\text{Fe}_2)\text{O}_5$ shows the strong asymmetry of the trigonal bipyramid. Iron was found to be preferentially located on the Mo(2) site. Bismuth atoms in the $x = 0.10$ and $x = 0.30$ compositions exhibit distorted coordination environments reflecting the stereochemical activity of the $6s^2$ lone pair of electrons. Trigonal and four pyramidal coordination environments are observed, representative examples of which are shown in Fig. 6b. Bi(7) located centrally between four $[\text{Bi}_{12}\text{O}_{14}]_n$ columns shows a trigonal pyramidal coordination (Fig. 6b) and forms two $(\text{MoO}_4)\text{--Bi}(\text{MoO}_4)\text{--}$ chains along the b -axis (Fig. 6c,d). Just as at room temperature, only one $(\text{MoO}_4)\text{--Bi}(\text{MoO}_5)\text{--}$ chain is observed. Forming such chains can affect the MoO_n polyhedral motion, which provide ionic transport (Holmes model of conductivity [13]) and influence the conductive properties.

Morphology and composition

Representative electron micrographs of powdered and ceramic samples are shown in Fig. 7. SEM micrographs of powdered samples show a homogenous distribution of large and small grains (Fig. 7a), with grain sizes in the range $\sim 0.1\text{--}5\ \mu\text{m}$ for all samples. After sintering of pellets, grain sizes increase to the range $\sim 1\text{--}50\ \mu\text{m}$ and dense ceramic samples were formed (Fig. 7b). The majority of pores are isolated and have a spherical form.

Iron concentration in $\text{Bi}_{26}\text{Mo}_{10-2x}\text{Fe}_{2x}\text{O}_{69-3x}$ shows good agreement with the theoretical values (Supplementary Information Table S8). The mean deviation of the experimental

Fig. 5 High-temperature diffractogram of $\text{Bi}_{26}\text{Mo}_{9.4}\text{Fe}_{0.6}\text{O}_{68.1}$ (upper) and topological representation (lower)

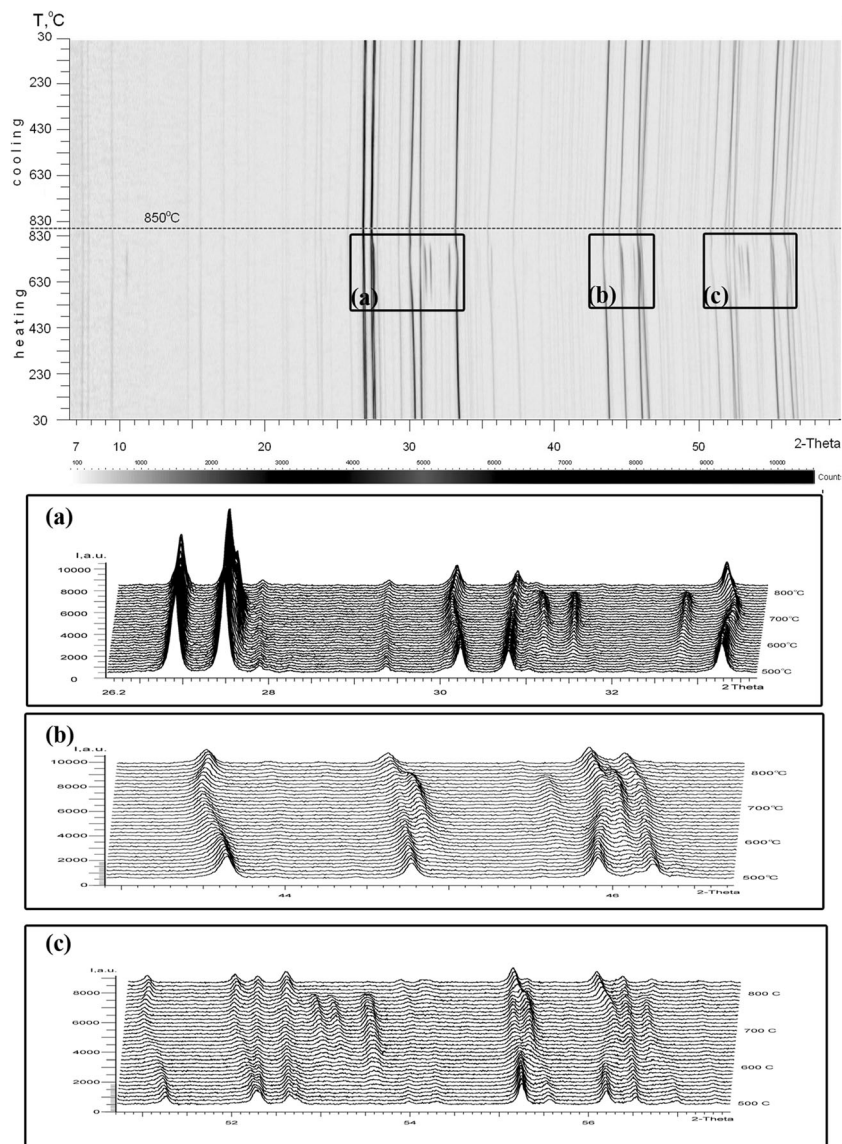


Fig. 6 **a** Trigonal bipyramidal coordination of Mo(2) and typical tetrahedral coordination of Mo; **b** trigonal and four pyramidal coordination of Bi; **c** coordination of isolated Bi(7) and $((\text{MoO}_4)\text{--Bi}(\text{MoO}_4)\text{--})_n$ chains; **d** structure of $\text{Bi}_{26}\text{Mo}_{9.4}\text{Fe}_{0.6}\text{O}_{68.1}$ at 650 °C

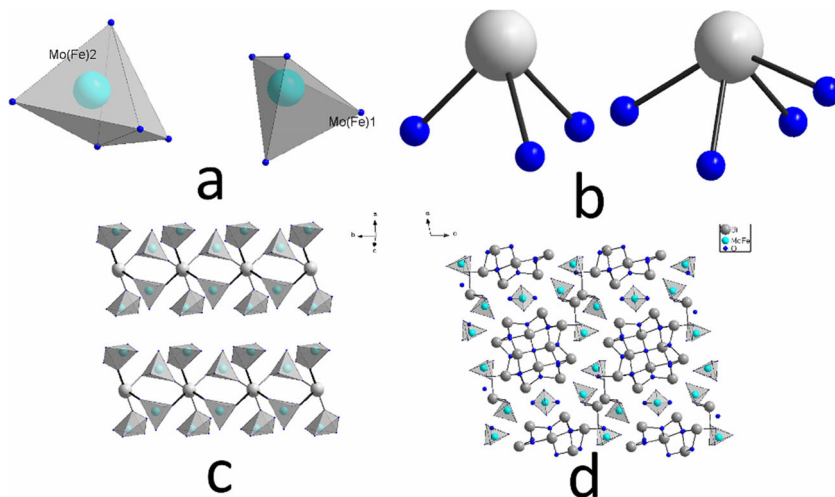


Table 2 Values of distortion indexes for $\text{Bi}_{26}\text{Mo}_{10-2x}\text{Fe}_{2x}\text{O}_{69-3x}$ at 650 °C

Compound	$\text{Bi}_{26}\text{Mo}_{9.8}\text{Fe}_{0.2}\text{O}_{68.7}$ Sp. gr. P2/c			$\text{Bi}_{26}\text{Mo}_{9.4}\text{Fe}_{0.6}\text{O}_{68.1}$ Sp. gr. P2/c			
	Polyhedron	DI (T-O)	DI (O-T-O)	DI (O-O)	DI (T-O)	DI (O-T-O)	DI (O-O)
Mo1(Fe1)O ₄		0.022	0.066	0.039	0.044	0.076	0.056
Mo2(Fe2)O ₅		0.076	0.218	0.165	0.083	0.212	0.174
Mo3(Fe3)O ₄		0.045	0.050	0.050	0.010	0.029	0.019

from the theoretical concentration is ~3–4%, which is less than method error (5%).

Magnetic measurements

In the present work, the magnetization curves of $\text{Bi}_{26}\text{Mo}_{10-2x}\text{Fe}_{2x}\text{O}_{69-3x}$ ($x = 0.1, 0.3$) and magnetic susceptibility vs temperature curves were obtained (Fig. 8). For the $x = 0.10$ composition, typical paramagnetic properties were observed in the range 4–300 K. It is well known that iron exhibits several possible oxidation states, the most common of which are Fe^{2+} and Fe^{3+} . Additionally, iron exhibits several types of coordination environments and various spin states, i.e., low spin (LS), high spin (HS), and intermediate spin (IS). For Fe^{3+} , two different spin states are possible, i.e., the high-spin state $t_{2g}^3e_g^2$ (oct.) or $e_g^3t_{2g}^2$ (tetr.) ($S = 5/2$) and the low-spin $t_{2g}^5e_g^0$ (oct.) ($S = 1/2$). Fe^{2+} can have three different spin states, i.e., the high-spin state $t_{2g}^4e_g^2$ (oct.) or $e_g^3t_{2g}^3$ (tetr.) ($S = 2$), the low-spin state $t_{2g}^6e_g^0$ (oct.) ($S = 0$), and the intermediate spin state $t_{2g}^5e_g^1$ (oct.) ($S = 1$) [27, 28]. Spin state transitions can be induced by varying the temperature, pressure, magnetic fields, chemical substitution, and gas adsorption [28] and are found in a wide range of materials. Theoretical magnetic moments μ_{eff} for selected spin states are given in the supplementary information as Table S9.

Magnetic susceptibility as a function of temperature for the $x = 0.10$ composition was fitted with the Curie–Weiss law $\chi_{\text{mol}} = \chi_0 + C/(T - \Theta)$; the obtained C parameter was $0.028 \text{ cm}^3 \text{ K mol}^{-1}$. The linear $M(H)$ plot at 300 K (inset in Fig. 8) confirms paramagnetic behavior for $\text{Bi}_{26}\text{Mo}_{9.8}\text{Fe}_{0.2}\text{O}_{68.7}$. Deviation from linearity for $M(H)$ at 3 K is the result of saturation effects and is typical for

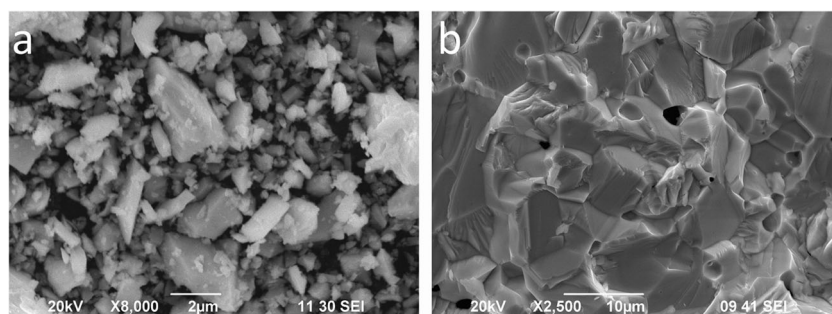
paramagnetic materials at low temperatures. The μ_{eff}^2 was calculated from the Curie constant and was $2.23 \mu_B^2$.

Several simple models of different iron ion mixtures were assumed: (1) $\text{Fe}^{2+}(\text{LS}) + \text{Fe}^{2+}(\text{HS})$; (2) $\text{Fe}^{2+}(\text{LS}) + \text{Fe}^{3+}(\text{LS})$; (3) $\text{Fe}^{2+}(\text{LS}) + \text{Fe}^{3+}(\text{HS})$. The molar concentration of each ion type was calculated from Eq. (2) (orbital magnetic moment for $\text{Fe}^{2+}(\text{HS})$ was not taken into account) and the results are shown in Table 3. It should be noted that such a low value of the magnetic moment can be considered as a unique example of $\text{Fe}^{2+}(\text{LS})$ stabilization in inorganic compounds induced by chemical substitution rather than temperature and pressure.

For $\text{Bi}_{26}\text{Mo}_{9.4}\text{Fe}_{0.6}\text{O}_{68.1}$, typical paramagnetic properties were observed in the range 2–250 K and even lower values of μ_{eff}^2 were obtained ($C = 0.033 \text{ cm}^3 \text{ K mol}^{-1}$; $\mu_{\text{eff}}^2 = 0.88 \mu_B^2$) (Fig. 9). This suggests that, despite the fact that the $\chi_{\text{mol}}(T)$ dependencies are well described with the Curie–Weiss law, the model of non-interacting localized moments does not adequately describe the magnetic properties of $\text{Bi}_{26}\text{Mo}_{10-2x}\text{Fe}_{2x}\text{O}_{69-3x}$. We can assume that in the systems under consideration, in addition to separate paramagnetic centers, there are exchange-coupled clusters with zero magnetic moment [27]. An alternative assumption could be the possibility of crossover from localized to itinerant electronic behavior associated with bond-length fluctuations [28] or the presence of Fe^{2+} with a low-spin spin state. This problem requires further study.

For the $x = 0.30$ composition, besides an anomalously low magnetic moment, a reversible magnetic transition was detected at ~250 K. It manifests itself in the growth of the magnetic susceptibility (inset in Fig. 9), as well as in the appearance of the hysteresis loops. The observed magnetic effect may be due

Fig. 7 SEM images of $\text{Bi}_{26}\text{Mo}_{9.6}\text{Fe}_{0.4}\text{O}_{68.4}$: **a** powder, secondary electron imaging, scale 1:8000; **b** ceramic pellet cross-section, backscattering electron imaging, scale 1:2500



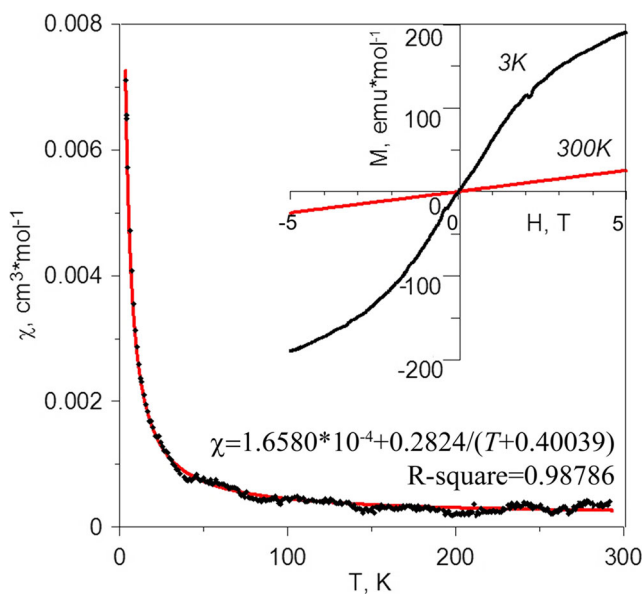


Fig. 8 Magnetic susceptibility for the $x = 0.10$ composition, as a function of temperature, fitted with the Curie–Weiss law. Magnetization curves for the $x = 0.10$ composition are shown at inset

to thermally induced ferromagnetism in band systems with a paramagnetic ground state [29] or it could be associated with a phase transition. In any case, judging by the magnetic saturation values, one can assume weak ferromagnetism or canting is present. This may well be associated with additional peaks in the high-resolution neutron data (absent in the X-ray data), which can be indexed through a doubling of the a and b parameters to give a $2a \times 2b \times c$ supercell (Supplementary Information Fig. S4). This superlattice might be associated with either or both ordering in the oxide ion sublattice and weak ferromagnetism.

Electrical conductivity

Fitting of A.C. impedance spectra was used to study the electrical behavior of compositions in the present system. Typical impedance spectra and model equivalent circuits are shown in Fig. 10. Two basic types of impedance curves were seen at low and high temperatures. In high-temperature spectra (> ca. 550 °C), a single broadened semicircle was observed with a non-zero high-frequency intercept on the real axis. This semicircle corresponds to the electrode electrolyte interface, with the high-frequency interface R0 corresponding to the total resistance of the electrolyte. Two R-CPE elements were used to model the semicircle, with typical capacitance values of ca.

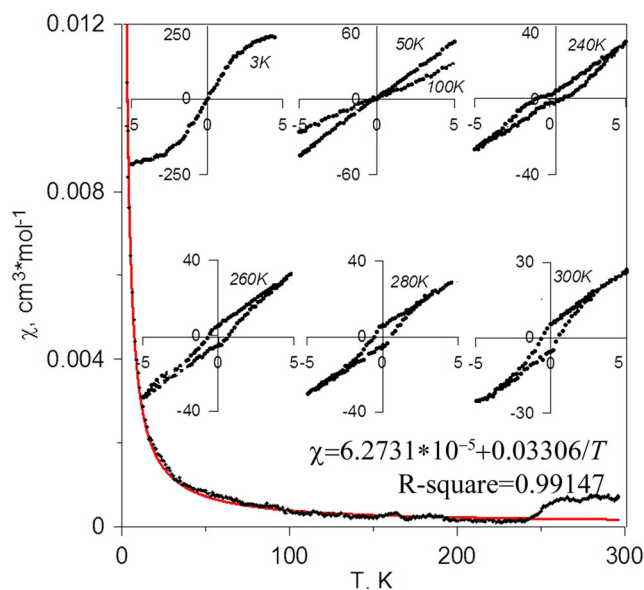


Fig. 9 Magnetic susceptibility as functions of temperature fitted with Curie–Weiss law for $x = 0.30$ composition; magnetization curves for $x = 0.30$ composition are shown at inset

10^{-4} – 10^{-6} F, characteristic of electrochemical processes at the electrode-electrolyte interface [30]. For spectra obtained at lower temperatures, a semicircle corresponding to the combined bulk and grain boundary resistances is observed and was fitted using a single R-CPE element, with the low-frequency end of the semicircle R1 corresponding to the total resistance of the electrolyte. Capacitance values for this high-frequency semicircle were in the range ca. 10^{-11} – 10^{-10} F, typical of grain boundary resistances in oxide systems [30]. For these low-temperature spectra, the electrode electrolyte interface response was modeled using a single R-CPE element and a Warburg component. The separation of total resistance into bulk and grain boundary components was not possible.

Arrhenius plots of total conductivity are presented in Fig. 11. For the $x = 0.0$ and 0.1 compositions, the plots consists of two linear regions at high and low temperatures, for the $x = 0.2$ and 0.3 compositions only one linear region is observed. The change of slope at ~ 300 °C for the $x = 0.1$ composition corresponds reasonably well with the diffraction results, which show the triclinic to monoclinic phase transition. For the $x = 0.2$ and $x = 0.3$ compositions, phase transition temperature is less than temperature range of electrical conductivity measurements and slight deviations from linearity are caused only by kinetic restraints at low temperatures described in [31].

Table 3 Molar concentration of different types of iron ions calculated in two-component models

Model	$\text{Bi}_{26}\text{Mo}_{9.8}\text{Fe}_{0.2}\text{O}_{68.7}$	$\text{Bi}_{26}\text{Mo}_{9.4}\text{Fe}_{0.6}\text{O}_{68.1}$
Fe^{+2} (LS)+ Fe^{+2} (HS)	91% Fe^{+2} (LS)+9% Fe^{+2} (HS)	96% Fe^{+2} (LS)+4% Fe^{+2} (HS)
Fe^{+2} (LS)+ Fe^{+3} (LS)	26% Fe^{+2} (LS)+74% Fe^{+3} (LS)	70% Fe^{+2} (LS)+30% Fe^{+3} (LS)
Fe^{+2} (LS)+ Fe^{+3} (HS)	94% Fe^{+2} (LS)+6% Fe^{+3} (HS)	97% Fe^{+2} (LS)+3% Fe^{+3} (HS)

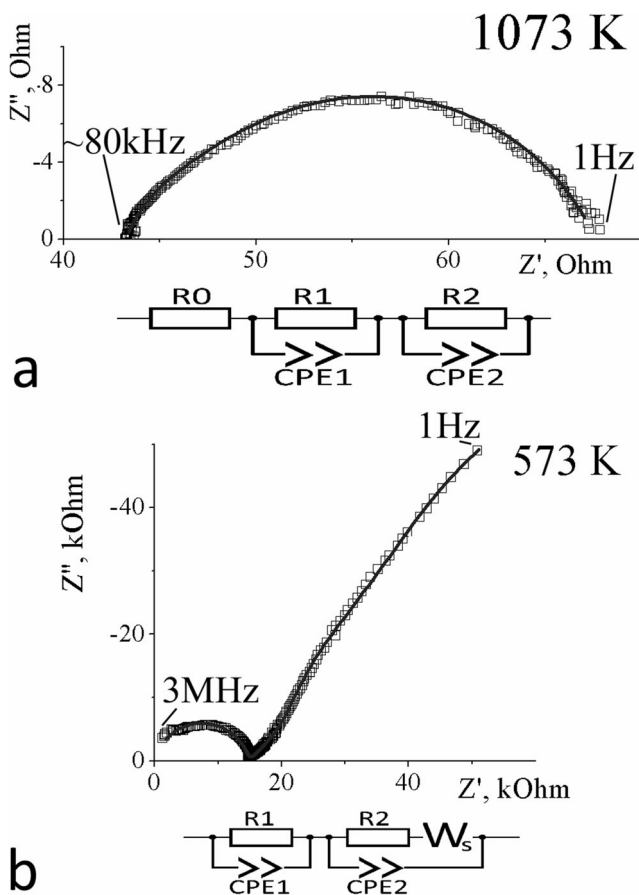


Fig. 10 Typical impedance spectra of iron-substituted bismuth molybdate (symbols) and model circuits and model spectra (line). **a** At high-temperature range. **b** Low-temperature range

The difference between triclinic and monoclinic structures affects the electrical conductive properties. The Holmes model [13] of conductivity in $\text{Bi}_{26}\text{Mo}_{10}\text{O}_{69}$ assumes three types of oxygen ion transfer: (1) oxygen ion motion using rotation of the Mo-O polyhedra (from room temperature to ca. 200 °C); (2) motion involving occupied and empty oxygen interstitial

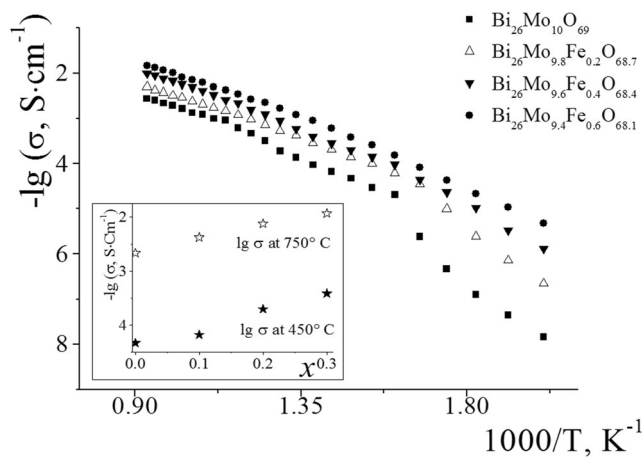


Fig. 11 Arrhenius plots of total conductivity of $\text{Bi}_{26}\text{Mo}_{10-2x}\text{Fe}_{2x}\text{O}_{69-3x}$ and concentration dependences of $\lg(\sigma)$ at 450 and 750 °C (inset)

sites + the MoO_4 tetrahedra rotational motion (~ 200 °C—phase transition temperature); (3) rotational motion of the Mo-O polyhedra + motion involving oxygen interstitial sites + motion involving oxygen atoms from the Bi-O columns (above the phase transition temperature) [13]. In general, this model does not describe the location of any interstitial oxygen sites. Observed $(\text{MoO}_4)-(\text{MoO}_5)$ moieties formed with Fe doping or $[(\text{MoO}_4)-\text{Bi}(\text{MoO}_4)]_n$ chains along the y -axis formed with temperature can affect the mentioned types of motion. Thus, the observed structure changes correlate with variations of electrical conductivity of the triclinic modification and the monoclinic phase and increase of conductivity with dopant concentration.

Conclusions

The $\text{Bi}_{26}\text{Mo}_{10-2x}\text{Fe}_{2x}\text{O}_{69-3x}$ solid solution was investigated. The solid solution limit was found to be around $x = 0.30$, with compositions crystallizing in triclinic symmetry. The unit cell volume was shown to decrease with increasing value of x associated with the loss of oxide ions from between the columns. SEM investigations of $\text{Bi}_{26}\text{Mo}_{10-2x}\text{Fe}_{2x}\text{O}_{69-3x}$ show a homogenous distribution of large and small grains; after sintering of pellets dense, ceramic samples were formed. Iron concentration in the $\text{Bi}_{26}\text{Mo}_{10-2x}\text{Fe}_{2x}\text{O}_{69-3x}$ determined by chemical analysis showed good agreement with the theoretical values.

The structure of $\text{Bi}_{26}\text{Mo}_{10-2x}\text{Fe}_{2x}\text{O}_{69-3x}$ is triclinic at room temperature and approaches monoclinic symmetry with increasing x -value. At $x = 0.10$, additional superlattice peaks are evident in the neutron diffraction data that can be indexed through a doubling of the a -axis. This superlattice may be associated with ordering in the oxide ion sublattice and/or weak magnetic ordering.

The structure of the triclinic phase was modeled in the non-centrosymmetric space group $P1$. The 69th oxygen position in the $x = 0.10$ and $x = 0.30$ compositions was found to be in a different position than to that proposed by Ling et al. [12] for the parent compound but similarly resulted in a distorted trigonal bipyramidal coordination for Mo [12]. Iron was found to be preferentially located on the Mo sites. The molybdate polyhedra show increasing distortion away from tetrahedral geometry, with increase of x .

A change from triclinic to monoclinic symmetry occurs between 300 and 350 °C for the $x = 0.10$ composition, while for the $x = 0.30$ composition, this transition occurs below ~ 250 °C. Above ca. 600 °C, phase separation occurs with the appearance of Bi_2MoO_6 and Fe_2O_3 in the diffraction patterns. This phase separation is seen only on initial heating, leaving the overall stoichiometry of the principal phase relatively unaffected. In the monoclinic phase at 650 °C, the 69th oxide ion again allows for a distorted trigonal bipyramidal coordination for

molybdenum. The $\text{Mo}(\text{Fe})\text{O}_n$ polyhedra are less distorted than those at room temperature. At 650 °C, a bismuth atom ($\text{Bi}(7)$) is located centrally between four $[\text{Bi}_{12}\text{O}_{14}]_n$ columns and forms chains between the molybdate polyhedral which can affect MoO_n polyhedral motion, believed to be responsible for the ionic transport in this system. The triclinic to monoclinic phase transition is reflected in Arrhenius plots of conductivity with change in activation energy. The variation of electroconductive properties in $\text{Bi}_{26}\text{Mo}_{10-2x}\text{Fe}_{2x}\text{O}_{69-3x}$ ascribed to structural changes such as formation of (MoO_4) – (MoO_5) moieties or $[(\text{MoO}_4)\text{–Bi}(\text{MoO}_4)]_n$ chains.

$\text{Bi}_{26}\text{Mo}_{10-2x}\text{Fe}_{2x}\text{O}_{69-3x}$ exhibits low magnetic susceptibility, with a reversible magnetic transition at ~250 K for the $x = 0.30$ composition. The observed magnetic effect may be due to thermally induced ferromagnetism or a possible phase transition.

Acknowledgements We are grateful to the STFC for beamtime at the ISIS Facility, Rutherford-Appleton Laboratory. Our thanks to Dr. Kevin Knight at the ISIS facility for his help in neutron data collection and Dr. R.M. Wilson at Queen Mary University of London for his assistance in X-ray data collection.

Funding information We also wish to acknowledge support from the Ural Federal University Development Programme for funding. The work was supported by the Russian Fund for Basic Research grant no. 16-33-60026 and the Royal Society International Exchanges Programme, grant no. IE140208.

References

- Wachsman ED, Lee KT (2011) Lowering the temperature of solid oxide fuel cells. *Science* 334:935–939
- Rolle A, Vannier RN, Giridgaran N, Abraham F (2005) Structural and electrochemical characterisation of new oxide ion conductors for oxygen generating systems and fuel cells. *Solid State Ionics* 176:2095–2103
- Sprenger P, Kleis W, Grunwaldt J-D (2017) Recent advances in selective propylene oxidation over bismuth molybdate based catalysts: synthetic, spectroscopic, and theoretical approaches. *ACS Catal* 7:5628–5642
- Moro-Oka Y, Ueda W (1994) Multicomponent bismuth molybdate catalyst: a highly functionalized catalyst system for the selective oxidation of olefin. *Adv Catal* 40:233–273
- Snyder TP, Hill CG Jr (1989) The mechanism for the partial oxidation of propylene over bismuth molybdate catalysts. *Cat Rev* 31:43–95
- Vannier RN, Mairesse G, Abraham F, Nowogrocki G (1996) $\text{Bi}_{26}\text{Mo}_{10}\text{O}_8$ solid solution type in the Bi_2O_3 – MoO_3 – V_2O_5 ternary diagram. *J Solid State Chem* 122:394–406
- Abraham F, Boivin JC, Mairesse G, Nowogrocki G (1990) The bimevox series: a new family of high performances oxide ion conductors. *Solid State Ionics* 40-41:934–937
- Takahashi T, Iwahara H, Nagaj Y (1972) High oxide ion conduction in sintered Bi_2O_3 containing SrO, CaO or La_2O_3 . *J Appl Electrochem* 2:97–104
- Buttrey DJ, Vogt T, Yap GPA, Rheingold AL (1997) The structure of $\text{Bi}_{26}\text{Mo}_{10}\text{O}_{69}$. *Mater Res Bull* 32:947–962
- Galy J, Enjalbert R, Rozier P, Millet P (2003) Lone pair stereoactivity versus anionic conductivity. Columnar structures in the Bi_2O_3 – MoO_3 system. *Solid State Sci* 5:165–174
- Vila E, Landa-Canovas RA, Galy J (2007) $\text{Bi}_{2n+4}\text{Mo}_n\text{O}_{6(n+1)}$ with $n = 3, 4, 5, 6$: a new series of low-temperature stable phases in the mBi_2O_3 – MoO_3 system ($1.0 \leq m \leq 1.7$): structural relationships and conductor properties. *J Solid State Chem* 180:661–669
- Ling CD, Miller W, Johnson MR, Richard D, Rols S, Madge J, Evans IR (2012) Local structure, dynamics, and the mechanisms of oxide ionic conduction in $\text{Bi}_{26}\text{Mo}_{10}\text{O}_{69}$. *Chem Mater* 24:4607–4614
- Holmes L, Peng L, Heinmaa I, O'Dell LA, Smith ME, Vannier RN, Grey CP (2008) Variable-temperature 17O NMR study of oxygen motion in the anionic conductor $\text{Bi}_{26}\text{Mo}_{10}\text{O}_{69}$. *Chem Mater* 20:3638–3648
- Bastide B, Enjalbert R, Salles P, Galy J (2003) Ionic conductivity of the oxide family $\text{Bi}[\text{Bi}_{12}\text{O}_{14}][(\text{Mo},\text{M})\text{O}_4]_5$ with $\text{M}=\text{Li}, \text{Mg}, \text{Al}, \text{Si}, \text{Ge}$ and V . *Solid State Ionics* 158:351–358
- Vannier RN, Danze S, Nowogrocki G, Huvy M, Mairesse G (2000) A new class of mono-dimensional bismuth-based oxide anion conductors with a structure based on $[\text{Bi}_{12}\text{O}_{14}]_\infty$ columns. *Solid State Ionics* 136-137:51–59
- Galy J, Salles P, Rozier P, Castro A (2006) Anionic conductors $\text{Ln}_{2/3}[\text{Bi}_{12}\text{O}_{14}][(\text{Mo},\text{M})\text{O}_4]_5$ with $\text{Ln} = \text{La}, \text{Nd}, \text{Gd}, \text{Ho}, \text{Yb}$. Synthesis–spark plasma sintering–structure–electric properties. *Solid State Ionics* 177:2897–2902
- Mikhaylovskaya ZA, Buyanova ES, Morozova MV, Petrova SA, Nikolaenko IV (2017) Mn-doped $\text{Bi}_{26}\text{Mo}_{10}\text{O}_{69-d}$: synthesis and characterization. *Ionics* 23:1107–1114
- Larson AC, Von Dreele RB (2004) General structure analysis system (GSAS), report LAUR 86-748. Los Alamos national laboratory, Los Alamos, New Mexico
- Bereciartua PJ, Zuniga FJ, Perez-Mato JM, Petricek V, Vila E, Castro A, Rodriguez-Carvajal J, Doyle S (2012) Structure refinement and superspace description of the system $\text{Bi}_{2(n+2)}\text{Mo}_n\text{O}_{6(n+1)}$ ($n=3, 4, 5$ and 6). *Acta Crystallogr Sect B: Struct Sci* 68:323–340
- Buttrey DJ, Jefferson DA, Thomas J (1986) Characterization of a new bismuth molybdate phase— $\text{Bi}_{38}\text{Mo}_7\text{O}_{78}$. *Mat Res Bull* 21:739–744
- Shannon RD (1976) Revised effective ionic radii and systematic studies of interatomic distances in halides and chalcogenides. *Acta Crystallogr A* 32:751–767
- Hamilton WC (1965) Significance tests on the crystallographic R factor. *Acta Crystallogr* 18:502–510
- Evans IR, Howard JAK, Evans JSO (2005) The crystal structure of $\alpha\text{-La}_2\text{Mo}_2\text{O}_9$ and the structural origin of the oxide ion migration pathway. *Chem Mater* 17:4074–4077
- Baur WH (1974) The geometry of polyhedral distortions. Predictive relationships for the phosphate group. *Acta Cryst B* 30:1195–1215
- Buttrey DJ, Vogt T, Wildgruber U, Robinson WR (1994) Structural refinement of the high temperature form of Bi_2MoO_6 . *J Solid State Chem* 111:118–127
- Blake RL, Hessevick RE, Zoltai T, Finger LW (1966) Refinement of hematite structure. *Am Mineral* 51:123–129
- Weihe H, Güdel HU (1997) Angular and distance dependence of the magnetic properties of oxo-bridged iron(III) dimers. *J Am Chem Soc* 119:6539–6543
- Goodenough JB, Rivadulla F (2005) Bond-length fluctuations in transition-metal oxides. *Modern Phys Lett B* 19:1057–1081
- Levitin RZ, Markosyan AS (1988) Itinerant metamagnetism. *Adv Phys Sci (Physics-Uspekhi)* 31:730–749
- Irvine JTS, Sinclair DC, West AR (1990) Electroceramics: characterization by impedance spectroscopy. *Adv Mater* 2:132–138
- Fonseca FC, Steil MC, Vannier RN, Mairesse G, Muccillo K (2001) Grain-sized influence on the phase transition of $\text{Bi}_{26}\text{Mo}_9\text{WO}_{69}$: an X-ray diffraction and impedance spectroscopy study. *Solid State Ionics* 140:161–171